A&A 676, A36 (2023)
https://doi.org/10.1051/0004-6361/202346304

Astronomy & Astrophysics
Special issue

Solar Orbiter First Results (Nominal Mission Phase)

First results from the Solar Orbiter Heavy Ion Sensor

S. Livi[1,2], S. T. Lepri[2], J. M. Raines[2], R. M. Dewey[2], A. B. Galvin[8], P. Louarn[7], M R. Collier[4], F. Allegrini[1], B. L. Alterman[1], C. M. Bert[2], R. Bruno[11], D. J. Chornay[4], R. D'Amicis[11], T. J. Eddy[2], L. Ellis[8], E. Fauchon-Jones[10], A. Fedorov[7], I. Gershkovich[2], J. Holmes[2], T. S. Horbury[10], L. M. Kistler[8], H. Kucharek[8], N. Lugaz[8], T. Nieves-Chinchilla[12], H. O'Brien[10], K. Ogasawara[1], C. J. Owen[9], M. Phillips[1], K. Ploof[2], Y. J. Rivera[3], S. A. Spitzer[2], T. J. Stubbs[5], and P. Wurz[6]

(Affiliations can be found after the references)

Received 2 March 2023 / Accepted 10 May 2023

ABSTRACT

Aims. Solar Orbiter launched in February 2020 with the goal of revealing the connections between the Sun's interior, atmosphere, and the heliosphere. The Solar Orbiter Heavy Ion Sensor (HIS) is a time-of-flight ion mass spectrometer dedicated to measuring heavy ions in the solar wind.
Methods. We present an overview of the first measurements of heavy ion composition from HIS, reviewing the methods used to transform the spectra obtained on board into scientific data products and examining two solar wind case studies as well as the statistical properties of the heavy ion composition observed by HIS. We also carried out a comparison with prior measurements of heavy ions at L1.
Results. The HIS data set provides the first mass- and charge-resolved heavy ion measurements in the inner heliosphere.
Conclusions. These high temporal resolution data have the potential to transform our understanding of the connections between the solar wind and its origin at the Sun, as well as the interaction between the solar wind and the environment around planets, comets, and in the interstellar medium.

Key words. solar wind – Sun: heliosphere – Sun: general – Sun: particle emission

1. Introduction

Solar Orbiter launched in February 2020 with the goal of providing a groundbreaking combination of remote and in situ measurements of the Sun in and out of the solar ecliptic plane. The mission's primary science goal is to understand the connections between the Sun and heliosphere and to help answer outstanding science questions in solar and heliospheric physics (Müller et al. 2020; Owen et al. 2020). These questions include the origins of the solar wind plasma and magnetic field, the drivers of heliospheric variability and radiation, and the generation of the solar dynamo. The solar wind originates in the million degree solar corona and expands out supersonically into the heliosphere, exposing all Solar System bodies to a continuous flux of charged particles (Ogilvie et al. 1980). While the solar wind drives space weather and strongly influences the near-Earth space environment as well as that of other planets, the nature of the solar wind and its origin are still unresolved (Viall & Borovsky 2020 and references therein). In particular, the details of the solar wind connection back into the solar corona remain difficult to constrain to specific sources. Yet these connections are of particular importance with regard to understanding the Sun's influence throughout the heliosphere.

The Solar Orbiter payload is outfitted with a combination of remote and in situ instruments, including the Solar Wind Analyser (SWA) instrument suite. SWA is a suite of particle sensors dedicated to measuring thermal and suprathermal solar wind plasma including electrons, protons, alphas, and heavy ions (Owen et al. 2020). The Heavy Ion Sensor (HIS) is one of three sensors that make up the SWA suite, in addition to the Electron Analyser System (EAS) and the Proton and Alpha Sensor (PAS). HIS was proposed and developed by an international team led by Southwest Research Institute (SwRI) with contributions from the University of Michigan, the University of New Hampshire, NASA Goddard Spaceflight Center (GSFC), and the Research Institute for Astrophysics and Planetology (IRAP) in Toulouse, France.

HIS provides detailed measurements of the chemical composition of the solar wind heavy ions in high temporal resolution, providing information on thermal ions from He to Fe, with their range of charge states, as well as on pickup ions (PUIs), including H^+, He^+, C^+, and O^+ and suprathermal ions (including protons) up to 75 keV e^{-1}. HIS scans its full energy-angle range at a 30 s time resolution in normal mode and 4 s time resolution in burst mode, allowing for characterization of velocity distribution functions, differential flux spectra, ion densities, thermal velocity, and bulk speed. A more in-depth discussion of instrument details, measurement concept, operations, and temporal resolution can be found in Owen et al. (2020).

Heavy ion measurements of the solar wind have been utilized to examine the local physical processes that occur in the heliosphere as well as to infer processes active in the solar atmosphere (Gloeckler et al. 1998; von Steiger et al. 2000; von Steiger & Zurbuchen 2011; Lepri et al. 2013; Laming et al. 2019). Because the freeze-in process sets ion charge-state abundances in the low corona (Bame et al. 1974), heavy ions can be used as tracers in the solar wind to link back to their origin within the corona. Heavy ion measurements can therefore be leveraged to track the thermal and acceleration history of the solar wind. For example, element fractionation, as observed through the relative abundances of different solar wind elements, indicates that different parcels of solar plasma can be

enhanced and depleted in their abundances relative to each other (von Steiger et al. 2000; Zurbuchen & Richardson 2006; Lepri et al. 2013; Zurbuchen et al. 2016; Lepri & Rivera 2021). This fractionation can be used to trace solar wind parcels to coronal source regions and examine physical processes in the chromosphere and the corona (Laming 2015; Laming et al. 2019; Rivera et al. 2022a). Additionally, solar wind source region can be differentiated by the varying prevalence of higher or lower charge states found in fast and slow solar wind (e.g., Zurbuchen et al. 2002; Zhao et al. 2009).

Transient events from the Sun also leave distinct imprints on the heavy ion composition of the solar wind. Coronal mass ejections (CMEs) involve the explosive release of magnetic energy and plasma from the Sun. Interplanetary CMEs (ICMEs) can be identified by their distinct solar wind characteristics, such as alpha/proton abundance ratios, velocity and density profiles, and charge state distributions (Lepri et al. 2001; Zurbuchen & Richardson 2006; Rakowski et al. 2007; Lynch et al. 2011; Zurbuchen et al. 2016; Rivera et al. 2019a). Studying these parameters can help establish links between coronal sources of CMEs and their in situ counterparts (e.g., Rivera et al. 2019b; Wurz et al. 2000; Uzzo et al. 2003). Measurements of solar wind ionization states have revealed the presence of highly ionized and heated material inside ICMEs (e.g., Bame et al. 1979; Galvin 1997; Gloeckler et al. 1998; Jian et al. 2018), which is taken as evidence of energy release during eruption (e.g., Lepri et al. 2001). This indicates that heavy ion measurements provide key constraints for models of solar wind origin and the release of CMEs (e.g., Rakowski et al. 2007; Lynch et al. 2011).

A growing body of research suggests that shocks accelerate ions out of an ambient suprathermal pool (Desai et al. 2003; Posner et al. 2004; Mason et al. 2008; Filwett et al. 2017, 2019; Zel'dovich et al. 2018, 2014), which has energies between the bulk solar wind and energetic particles. There are many open questions in this area because the instruments making the associated observations measure either the solar wind and the lowest end of the suprathermal range (e.g., ACE/SWICS) or they measure the upper end of the suprathermal range and energetic particles, both with a considerably lower temporal resolution than the timescales relevant for particle acceleration and heating (Mason et al. 1998; Desai & Giacalone 2016). There is also much to be learned regarding the spectral variation and evolution of so-called suprathermal tails (Yu et al. 2018). Having the energy spectra of accelerated particles from just above the solar wind thermal range to energetic particles allows for conclusions to be drawn regarding the actual acceleration mechanism at the start of the acceleration to energetic particles (Bamert et al. 2008). In addition, knowing the composition of the suprathermal particles and comparing them with the composition of the thermal plasma of the solar wind can offer clues about the origin of suprathermal ions. For example, in studying the event of May 1998 with SOHO/CELIAS/STOF, it was concluded that there is a significant contribution from interstellar pickup ions to the observed suprathermal ions (Bamert et al. 2002). By providing both composition and charge state observations at a high temporal resolution up to suprathermal energies, HIS provides the comprehensive observations necessary to properly characterize the acceleration and heating mechanisms associated with shocks, both interplanetary and CME-driven.

In addition to suprathermal particles, HIS observes PUIs embedded in the solar wind, which are created through the ionization of initially neutral particles through mechanisms such as electron impact ionization, photoionization, and charge exchange with the solar wind. Once the neutrals become ionized, they are accelerated (or picked up) by the solar magnetic field and begin to propagate radially with the solar wind, thus the designation of PUIs. These neutral particles can originate from various inner sources such as comets, interplanetary dust, and planetary atmospheres, while the bulk of PUIs observed in the solar wind originate from interstellar neutrals. These ions can be distinguished from the solar wind by their distinctive features in the velocity distributions, thus providing insights into their sources (Geiss et al. 1996; Gloeckler & Geiss 1998; Gilbert 2012; Gershman et al. 2013; Gilbert et al. 2015; Rivera et al. 2020), production mechanisms (Taut et al. 2015), and evolution of their velocity distributions (Drews et al. 2015, 2016). The interstellar PUIs also provide a method for determining the interstellar flow longitude (Möbius et al. 2015).

In this paper, we discuss the unique capabilities of HIS and present measurements of heavy ion composition observed during the initial phases of the mission. We focus on one full orbit of measurements, which represent the first mass- and charge-resolved observations of heavy ions in the inner heliosphere (0.28 to 1 AU). In Sect. 2, we give a description of the instrument, discussing principles of operation and providing relevant physical specifications. In Sect. 3, we detail the scientific data processing methods and settings used to convert the raw instrument measurements into the delivered heavy ion composition data set. We present several early events of interest that showcase the HIS instrument's capabilities in Sect. 4. In Sect. 5, we compare the statistical properties of the early HIS data to observations made by the ACE/SWICS spectrometer over the course of its lifetime. Finally, we discuss and summarize our key results in Sect. 6.

2. Instrument description

HIS is a time-of-flight (TOF) ion mass spectrometer dedicated to the measurement of the heavy ion composition and velocity distributions of the solar wind, extending from the thermal to suprathermal energy domains. HIS measurements span the bulk solar wind ions, PUIs, and suprathermal ions, resolving species ranging from He to Fe across most of their ionization or charge states. Figure 1 shows a cutaway view of the instrument. Due to the close approach to the Sun (0.28 AU), specialized thermal control is required, such as the HIS dedicated heat shield. Behind the heat shield, the entrance system consists of ion-steering (IS) deflector plates and a solar photon pass-through out the back of the instrument. The IS plates, in combination with the electrostatic analyzer (EA, comprised of nested partial hemispheres) are known as the EA-IS system. The EA-IS system selects incoming ions based on E/q as well as elevation angle. The EA-IS aperture also defines the azimuth field of view. The selected ions pass through a post-acceleration (PA) gap with nominal −25 keV potential before they enter the TOF telescope through a carbon foil. Forward emitted secondary electrons from the carbon foil are deflected onto the "start" microchannel plate (MCP) and backward emitted secondary electrons from the front of the solid state detectors (SSDs) are deflected onto the "stop" MCP to provide the TOF measurement, typically in the range of 10–100 nanoseconds. The array of SSDs also measure the total energy of each incident ion. Electronics inside the TOF telescope and the main electronics box record ion position, energy, timing, and pair ion and electron signals. The HIS field of view (FOV) spans a 96° in azimuth (AZ), from −30° to +66° parallel to Solar Orbiter's orbital plane. The azimuth is determined from the ID of either the triggered SSD detector or the impact location

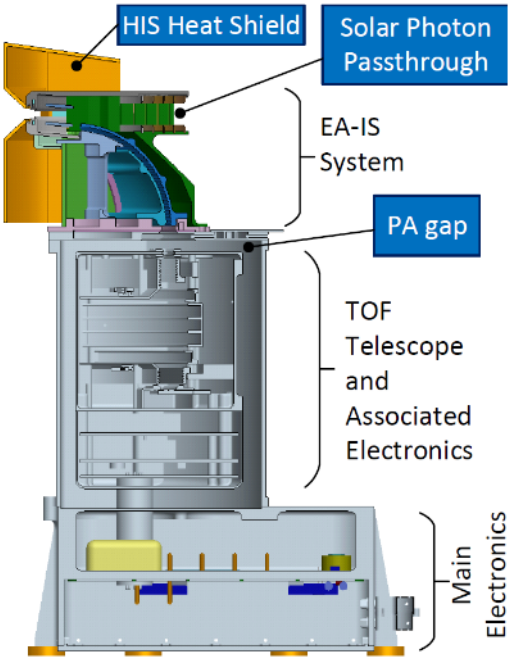

Fig. 1. Schematic of the HIS instrument with labels for the heat shield, solar photon pass-through, EA-IS system, TOF telescope and associated electronics, and the main electronics (adapted from Owen et al. 2020).

along the MCP anode. Ion steering provides the elevation (EL) of individual ions to a maximum of ±17° above and below Solar Orbiter's orbital plane and is determined through voltage selection on the deflector plates and ESA. Hence, HIS selects the energy-per-charge (E/q) and elevation angle and it directly measures the total energy (E), TOF, and azimuth angle of incident ion. Together, these measurements enable the determination of an individual ion's mass and charge and the extended 3D velocity distributions of different ion species. A detailed description of the instrument and its principle of operation can be found in Owen et al. (2020).

3. Scientific data processing

HIS is capable of simultaneously identifying over 75 ion species in the solar wind based on measured E/q, TOF, and E, as well as elevation and azimuth angles for each incident ion. For each ion, these parameters and measurements are assembled into an "ion event word". Ion event words, also known as pulse-height analyzed (PHA) words, are the primary raw data product from the instrument. About 950 000 event words can be stored by HIS for each E/q scan (0.5–75 keV e^{-1}) in an event buffer, but only a small sample is actually telemetered to the ground due to downlink data volume limitations. The sample size is configurable by ground command. For the period addressed in this paper, it was set at 11 904 event words for each 30 s normal mode scan. This value represents about twice the number of event words available for a 2 h period on ACE/SWICS.

In the solar wind, heavy ion abundances can vary by orders of magnitude between He and individual species of heavier elements. To ensure a representative sample of heavy ions is obtained in each scan, a priority scheme has been implemented that preferentially prioritizes low abundance ions and deprioritizes abundant ions in a way that their true abundances can be reconstructed on the ground. This priority scheme is implemented in the flight software in three steps. First, ion events are classified into one of eight priority ranges that prioritizes less abundant ions (e.g., Fe) over the most abundant ions (e.g., He). Table 1 lists the eight priority ranges, the corresponding ions, and the adjustable parameters explained below, as flown during the January to June 2022 period. These priority ranges are defined as regions in (E/q, TOF, E)-space occupied by different ion species. Second, the ion words are stored in the event buffer. Ion events are stored sequentially as HIS steps through its 64 E/q values, scanning 16 ELs within each E/q step. Each priority has a dedicated portion of the event buffer indicated by its event buffer size. To avoid disproportionately filling the buffer with a few select ion species, each priority has a limit on the number of events that can be stored for a particular (E/q, EL) step, known as the input limit. Third, once an E/q scan is completed, random samples of ion events in each priority range, working from highest (range 0) to lowest (range 7) priority, are stored in telemetry (TM). These samples are known as TM samples. If there are fewer events in the buffer than available slots in telemetry for a given priority range, the excess TM sample slots are allotted to the next lower priority. Due to their low abundance and corresponding low flux over a 30 s E/q scan, priority ranges 1–3 are typically not filled. These excess TM sample slots are typically used for priority ranges 4 (O^{6+}) and 5 (He^{2+}). Alongside the ion event TM samples, a set of priority rates is also downlinked. These contain the number of events per (Priority range, EL, E/q) and allow for the renormalization of telemetered events on the ground, to account for the fraction of events not telemetered.

Substantial ground processing is required to compute heavy ion composition parameters from ion event words. Once on the ground, each individual ion event word is assigned to a particular ion species through a multi-step maximum likelihood estimator (MLE) process which removes overlap between the ions in a statistically robust way. This method was first implemented for ACE/SWICS (Shearer et al. 2014) and has been adapted for HIS. The current implementation accumulates ion events over incident angles. The preservation of incident angles will be implemented for a future version of the released data. The method operates on events from each E/q step independently and proceeds as follows. First, counts of ion events were grouped into a 2D histogram of digital TOF and E values, each of which range across 0–511 channels. Second, the probability distribution functions that describe where each ion species lands in TOF and E were constructed from 2D Gaussian curves. The centers and widths of these curves in TOF and E, which characterize the instrument forward model, were initially derived from a simple physics based model adjusted with ground calibration data. This model includes estimates of energy lost by an ion as it passes through the HIS carbon foil derived from Transport of Ions in Matter (TRIM) simulations (Allegrini et al. 2003; Ziegler 2004), as well as estimates of energy measured by the solid state detectors, taking into account the nuclear defect, detector efficiencies, and conversion from physical to digital units (Ipavich et al. 1978). Forward-modeled centers and widths were further refined by comparison to an accumulation of flight data over the entire January to June 2022 period. These model-data comparisons focus on well-separated or relatively abundant heavy ions (e.g., O^{6+}) and are then extrapolated to other ion species. Finally, the counts and probability distributions are fed through the MLE method that iteratively redistributes counts among the various species until an optimal solution is achieved. As HIS continues to operate, the increasing total volume of data will allow additional ions to be directly compared thus improving the accuracy of the MLE recovery. The output of the MLE algorithm produces

Table 1. Parameters in each of the eight HIS priority levels defining the behavior of the onboard ion event priority scheme as flown from January to June 2022.

Priority range	Ions	Event word input limit	Event word buffer size	Event word telemetry sample
0	PUI	400	100 250	1297
1	Fe^{6+} – Fe^{9+}	400	114 250	2695
2	Mg^{5+} – Mg^{12+} Si^{6+} – Si^{12+} Ne^{8+} – Ne^{10+} S^{6+} – S^{14+} Fe^{10+} – Fe^{20+}	400	100 502	2819
3	C^{4+} – C^{6+} N^{5+} – N^{6+} O^{5+}, O^{7+} – O^{8+}	400	116 250	3494
4	O^{6+}	100	2500	199
5	He^{2+} H^+ (>5 keV e^{-1})	100	5000	598
6	H^+ (<5 keV e^{-1})	100	10 000	598
7	Noise	100	10 000	598

Notes. The first column lists the designation of each priority range, the second column lists the associated ion species, the third column lists the input limit for the maximum allowed number of event words per elevation step, the fourth column lists the event buffer storage size limit in event words per complete scan onboard the spacecraft, and the fifth column lists the telemetry sample size limit in event words per complete scan for downlink to the ground. Each subsequent priority level may receive additional allowed event words for downlink in a given scan if the previous level has not saturated its telemetry sample limit.

vectors of counts at each E/q step for each ion species. These vectors can then be transformed into differential energy flux and 1D velocity distributions functions from which moments are computed by numerical integration to obtain density, bulk speed, and thermal speed within the spacecraft frame. Ratios and ratios of sums of these recovered densities are then used to calculate the composition parameters: charge state ratios, charge state distributions, and relative element abundances. The data are currently accumulated into 10 min (nominally 20 E/q scans) intervals (although this accumulation is flexible) for delivery to the Solar Orbiter Archive (SOAR).

Figure 2 illustrates a sample of unprocessed HIS measurements during an interplanetary shock on May 12, 2022[1]. In these measurements, no differentiation of individual ions has been made, so these E/q, E/q-TOF, and E-TOF spectra are each sums of all ions in the solar wind within the HIS E/q and FOV range. Panel (a) shows the number of triple-coincidence ion event words (i.e., both a valid TOF, including start and stop signals, and a valid E measurement) at each E/q value (summed over all ELs and azimuth) at the native 30 s E/q scan time. The dark gray region indicates that the instrument's proton avoidance had triggered, limiting the EA-IS voltages to prevent admittance of ions below a given E/q threshold into the instrument to preserve detector lifetimes (see Owen et al. 2020). The passage of a shock is evident in panel (a) just before 22:50 UTC by the sharp discontinuity in the spectra as the observed population shifts to higher energy per charge and the count distribution increases in intensity and broadens. The observed transitions correspond to increases in the bulk plasma speed, density, and temperature, respectively. We can see that after the shock the E/q distribution is broad and extends to the highest measured E/q values, whereas measurements taken upstream show a local maximum near 2 keV e^{-1} (solar wind He^{2+} ions) and a suprathermal component (>8 keV e^{-1}). The lack of a local maximum in flux in the shocked region is due to the proton avoidance mode limiting observations of the lower energy per charge range where the distribution would be expected to decline. This can be seen in panel (c), where the H^+ and He^{2+} flux is cut off in E/q. HIS recorded a gradual increase in suprathermal (>8 keV e^{-1}) counts just ahead of the shock as observed in both panels (a) and (b), as observed in Wind/STICS measurements by Posner et al. (2004). While the flux remains fairly steady before and after the shock, small fluctuations can be observed to occur on time scales around the 10 min resolution of the processed data. These small fluctuations will likely provide important information about heavy ion kinetics near shocks in future studies.

Figures 2b,c provide a closer look at plasma composition by showing two E/q-TOF spectra. Different ion species concentrate along different magenta curves, denoting different m/q values, as shown on the plot. Ions with $m/q = 1$ (H^+) are on the far left and ions with $m/q = 7$ are on the far right (e.g., Fe^{8+}). A diagonal dashed blue line depicts the (ground processing) threshold ($V_{sw} - 2V_{th}$) used to limit the accidental coincidences that could skew recovery of ion characteristics. The low-velocity cutoff was applied to the data during ground processing and used to separate solar wind counts from TOF accidentals that occur most often near the E/q peaks of H^+ and He^{2+}. Proton avoidance shows up in these panels as the grey shaded area, which is seen to shift to higher E/q after the shock passage. Panel (b) shows the E/q-TOF spectra immediately preceding the shock and panel (c) shows the spectra immediately following the shock, indicated by the orange boxes in panel (a). These histograms are constructed from 10-min accumulations of the 30 s E/q scans, equivalent to the time resolution of the currently released composition data set available in the SOAR. Different heavy ions are observed across a range of m/q values, with the solar wind concentrated in the region with peak fluxes along the curves. The peaks in m/q tend to lie along a

[1] Data are available at https://doi.org/10.7302/rt8v-6c70

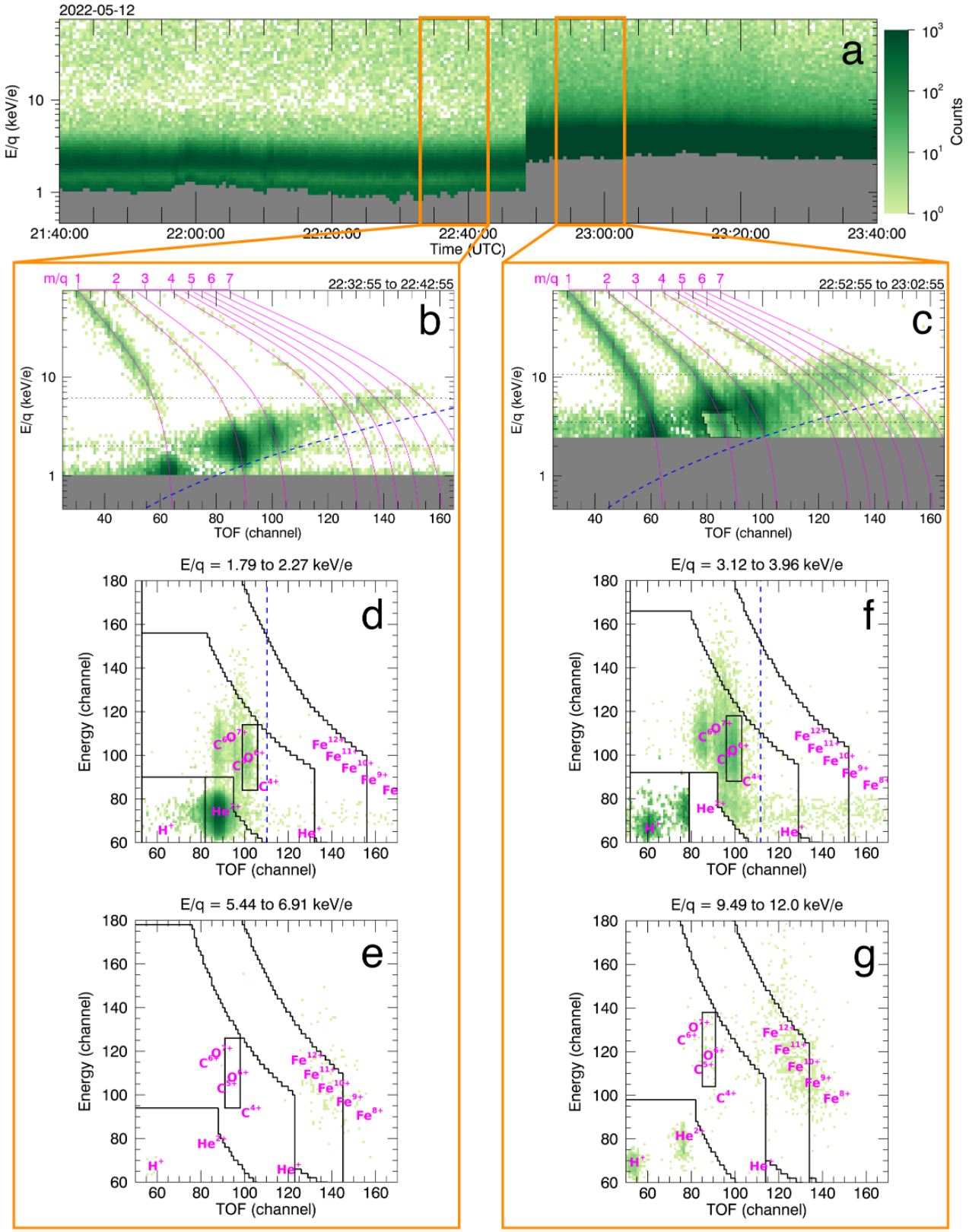

Fig. 2. HIS measurements about an interplanetary shock encountered by Solar Orbiter on 12 May 2022. Panel (a): HIS E/q spectra at native 30-s resolution over a 2 h interval. Panels (b),(c): E/q-TOF distributions accumulated over 10-min before and after the shock, corresponding respectively to the orange-outlined intervals in panel (a). Panels (d)–(g): E-TOF distributions at the peak E/q step for He^{2+} and other M/q = 2 ions (panels (d),(f)) and for Fe^{9+} (panels (e),(g)). The colorbar is consistent throughout all panels. Dark gray indicates E/q steps affected by the instrument's proton avoidance (panels (a),(c)), magenta corresponds to m/q (panels (b),(c)) and ion species (panels (d)–(g)), dashed blue lines are the velocity filter applied to the data panels (b)–(g), and thick black lines mark boundaries between priority ranges as listed in Table 1 panels (c)–(g)). Suprathermal trails for (left to right in TOF) H^{1+}, He^{2+}, and He^{1+} can be observed in panels (b),(c).

diagonal curve in E/q vs. TOF space, which is proportional to the solar wind velocity of the bulk plasma. Ions shift to higher E/q along these curves as the solar wind speed increases, as seen in panel (c). The general relationship between E/q, TOF, and solar wind velocity can be found in Gloeckler et al. (1998). Before the shock (panel (b)), each of the local maxima on the tracks peak at lower E/q and are narrower in their E/q extent than after the shock (panel (c)), where the higher bulk speed and increased temperature are apparent. Following the shock, there is a discontinuity near the $m/q = 2$ maximum, outlined in black. Here, the high He^{2+} density saturated the priority range 5 event buffer such that the buffer filled before proton avoidance triggered or the E/q scan finished. As a result, no event words from priority range 5 could be selected for telemetry in these E/q steps. The counts within this outlined region actually correspond to C^{6+} (also $m/q = 2$) that falls in priority range 3. The degeneracy of m/q highlights the importance of E measurements, shown in panels (d)–(g).

Figures 2d–g shows four E-TOF spectra. The E-TOF spectra were obtained for each E/q step. For solar wind ions with similar speeds, E/q is directly proportional to m/q, and the spectra shown in Figs. 2d–g correspond to the $m/q = 2$ (panels (d),(g)) and $m/q = 6$ (panels (e),(g)) peaks both before and after the shock. In these spectra, the forward model positions for notable ions are labeled in magenta. As can be seen in panels (d)–(g), the overlap between multiple species in E-TOF parameter space (e.g., near O^{6+}) necessitates the use of a maximum likelihood estimator (MLE) processing to disentangle these populations. The forward model centers, along with their corresponding widths (not shown), form the basis for the probability distributions that are input alongside the E-TOF distribution into the MLE processing as described above. In other areas of E-TOF parameter space, ions are more cleanly separated, such as between He^{2+} and C^{6+}. The priority ranges for each step are overlaid on the E-TOF spectra as thick black lines that have been optimized to collect different ion species. The saturation of priority range 5 after the shock is visible as the white space near the He^{2+} center at E/q ~ 3.5 keV e^{-1} (panel (f), TOF range 80–100 channels, E range 60–90 channels). Despite this saturation, onboard velocity distribution functions (VDFs; Owen et al. 2020) can be used to correct for the saturation in priority ranges 5–6. The TOF accidentals are visible in the E-TOF spectra extending off to the right of the H^+ and He^{2+} peaks in panels (d) and (f). Accidentals are most frequent with high-abundance and low-efficiency species. As such, accidentals are identified by their broad TOF distribution over energy channels near the H^+ and He^{2+} energy centers. The velocity filter shown in panels (b) and (c) appear here as vertical dashed blue lines in panels (d) and (f). Ion events to the right of these blue lines are removed from our analysis to prevent misassignment of these counts to other low-charge species (e.g., He^+).

As of this writing, the above methodology has been used to produce V01 of the HIS Level 3 composition data set, which is available at the SOAR. These data are available accumulated to 10 min temporal resolution. For V01, only the subset of the full composition products which could be produced at high quality were included (Table 2). For example, only charge states $8–12^+$ are included in the Fe charge state distributions. As more data are accumulated on the ground, additional charge states and composition data products will be added to this set and the data set released as subsequent version numbers. The full set of anticipated composition data products is described in Owen et al. (2020). Occasional data gaps will occur due to a variety of reasons: instrument-off, non-nominal operations, low data-confidence intervals. More detailed information on the data products can be found in the data release notes provided at the SOAR.

Table 2. HIS V01 composition data products, available at 600 s (10 min) time resolution.

Current data products
Elemental abundances
Fe^{6-20+}/O^{5-8+}
Ionic charge states
O^{7+}/O^{6+}
C^{6+}/C^{5+}
C^{6+}/C^{4+}
$\langle Q_O \rangle$
$\langle Q_C \rangle$
Ionic charge state distributions
$Q_i(O), i = 5, \ldots, 8$
$Q_i(C), i = 4, \ldots, 6$
$Q_i(Fe), i = 8, \ldots, 12$
Bulk properties
O^{6+} (v_{bulk}, $v_{thermal}$)

4. Example events

In this section, we present two intervals that feature heavy ion composition parameters for different solar wind structures. The same heavy ion parameters are plotted for both intervals in Figs. 3 and 4. Panel (a) shows magnetic field data from MAG (Horbury et al. 2020), including the magnetic field in RTN coordinates (B_R, B_T, B_N) as well as the magnitude ($|B|$); a data gap is present from 15:00 12 May – 04:20 13 May 2022. Panel (b) shows n_p, the proton density, from PAS, and panels (c),(d) show the PAS v_p, proton velocity, and $v_{p,th}$, thermal speed (black) along with the HIS $v_{O^{6+}}$ $v_{th;O^{6+}}$ in red. Panels (e)–(g) plot the C, O, and Fe charge state distributions, showing the relative abundances of individual ions. The black lines in panels (e),(f) are the average charge state values overlaid on the charge state distributions. Panels (h)–(j) show O^{7+}/O^{6+}, C^{6+}/C^{5+}, and C^{6+}/C^{4+}, respectively. Panel (k) shows Fe/O. We note that prior studies of $v_{O^{6+}}$ have shown strong correlation with $v_{He^{2+}}$, making it a good proxy for solar wind speed (Hefti et al. 1998). Hereafter, references to solar wind speed in the figures assume we are referring to $v_{O^{6+}}$.

The first example interval is shown in Fig. 3 for the period 12 to 13 May 2022, when Solar Orbiter was between ~0.802–0.807 AU. Between 22:00–23:00h UTC the plasma parameters (density and speed) indicate a relative strong ICME driven shock signature followed by the sheath region of compressed solar wind, marked by the first solid vertical red line. The ICME region (bounded by the vertical dashed black lines) is observed from 00:00–11:00 UTC on May 13, 2022. This interval is followed by a slow reverse shock propagating towards the Sun just before 12:00 UTC on 13 May 2022 (marked by the second solid vertical red line). The ICME interval is estimated to last from just after the sheath to just before the reverse shock on the trailing edge. Here, both the plasma density (panel (b)) and the proton thermal speed (panel (d)) decreases while the total magnetic field (panel (a)) and the proton speed (panel (c)) increase. This is a signature of a slow reverse shock. These discontinuities are weak and difficult to observe and to identify. More details of this type of discontinuity in the solar wind were first provided by Burlaga & Chao (1971).

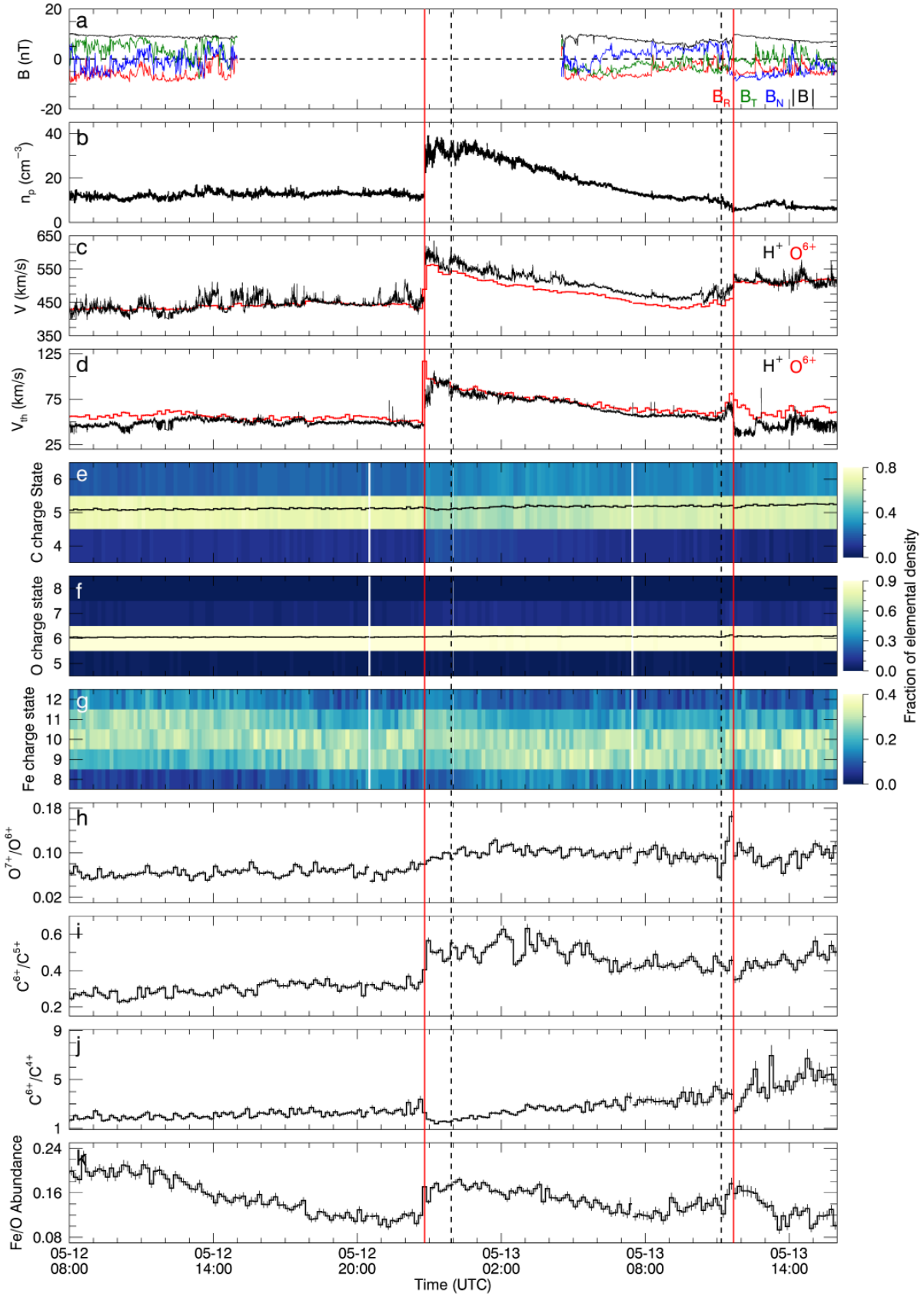

Fig. 3. In situ measurements of an event in the solar wind on 12 to 13 May 2022. (a) MAG magnetic field RTN components and magnitude, (b) PAS n_p, (c)–(d) PAS v_p and $v_{p,th}$ and HIS $v_{O^{6+}}$, and $v_{O^{6+},th}$, (e)–(g) elemental charge state distributions of C, O, Fe, (h)–(j) ion charge state ratios, and (k) Fe/O element abundance ratio. The first solid vertical red line marks the shock arrival time as observed by HIS. The ICME region is bounded vertical dashed black lines. A reverse shock is marked by the second solid vertical red line.

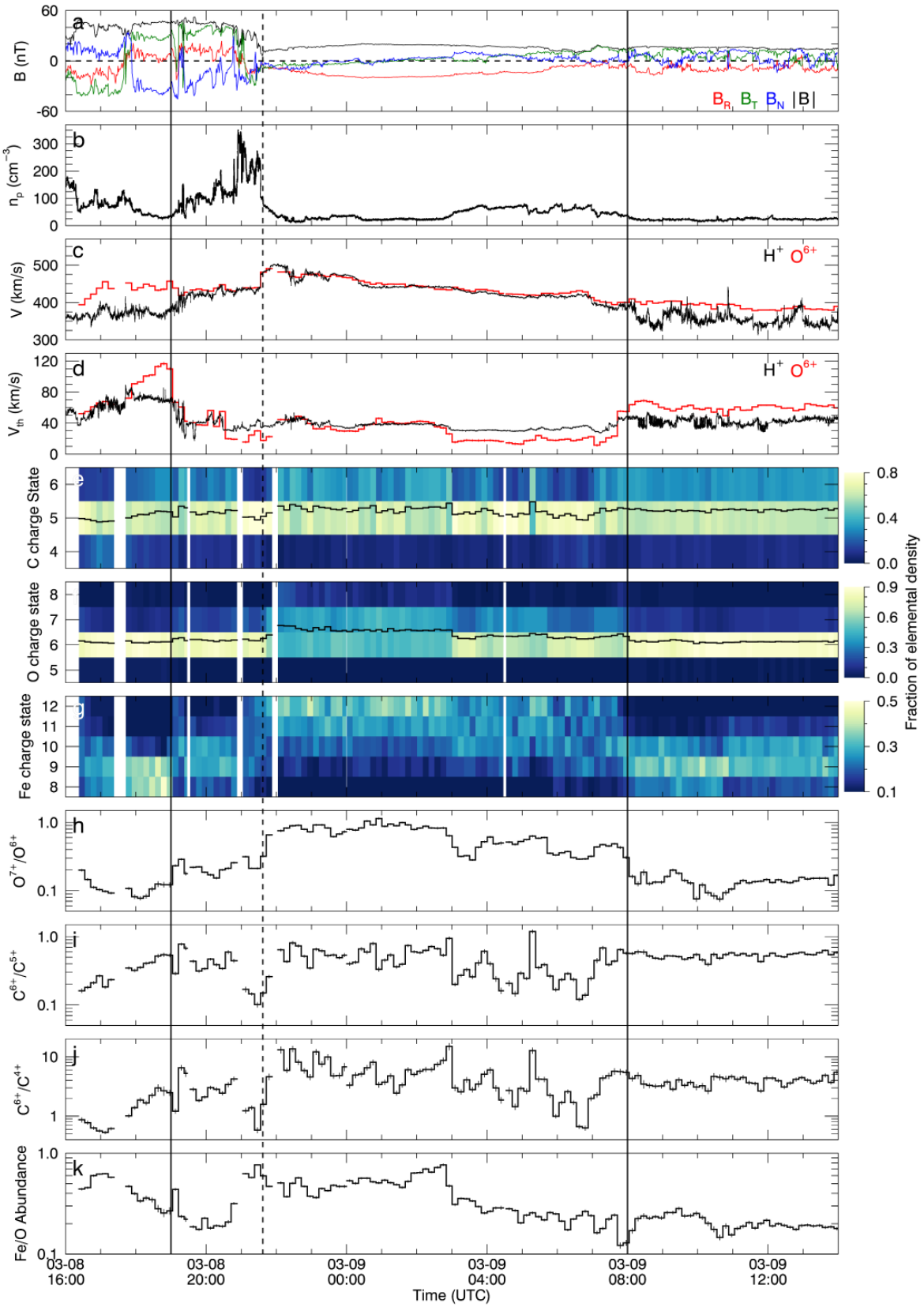

Fig. 4. In situ measurements of an ICME in the solar wind on March 8–9, 2022. (a) MAG magnetic field RTN components and magnitude, (b) PAS n_p, (c)–(d) PAS v_p and $v_{p,th}$ and HIS $v_{O^{6+}}$, and $v_{O^{6+},th}$, (e)–(g) elemental charge state distributions of C, O, Fe, (h)–(j) ion charge state ratios, and (k) Fe/O element abundance ratio. The ICME start is marked by the first vertical solid black line, with the magnetic obstacle arrival marked by the vertical dashed black line. The end of the ICME and magnetic obstacle are marked by a second vertical solid black line.

For more details on the association of reverse shocks and ICME evolution, we refer to Manchester et al. (2017, and references therein).

Figure 3 also includes the period shown above in Fig. 2. The interval begins with solar wind speeds near 425 km s^{-1} and a thermal speed of approximately 50–60 km s^{-1}, characterized by O^{7+}/O^{6+} ~0.06. A comparison of these values with literature values indicates that they fall within the range expected for quiet-Sun related solar wind near solar minimum; yet they are also similar to coronal hole related solar wind values during solar maximum (Zhao et al. 2017a). As this time period occurs during the ascending phase of the present solar cycle (source: WDC-SILSO, Royal Observatory of Belgium, Brussels), this value for O^{7+}/O^{6+} does not uniquely delineate the solar wind source region. However, the Fe/O ratio begins near 0.12, a value associated with slow solar wind (e.g., Wurz et al. 1999; Aellig et al. 1999; von Steiger & Zurbuchen 2011). While O^{7+}/O^{6+} has long been held as a standard marker of fast vs. slow solar wind (coronal hole vs. quiet Sun and active region sources of solar wind), C^{6+}/C^{4+} has been found to be a more robust marker of solar wind type as carbon tends to freeze-in lower in the corona (Landi et al. 2012). Due to the evidence from Fe/O and the higher C^{6+}/C^{4+} ratio, it seems that the region preceding the shock is slow solar wind of quiet Sun origin. The appearance of the shock at ~22:48 UTC is evident by the sharp increase in n_p, v_p, $v_{p,th}$, $v_{O^{6+}}$, and $v_{th;O^{6+}}$, which demonstrates the heating and acceleration of the O^{6+} velocity distribution across the shock. The composition parameters also shift after the shock. As the solar wind transitions to faster speeds, the O^{7+}/O^{6+} and C^{6+}/C^{5+} ratios shift up indicating that HIS is still sampling wind that originates from outside of coronal holes, perhaps from an active region (Zhao et al. 2009). Somewhat counter-intuitively, the C^{6+}/C^{4+} ratio shifts down indicating changes to the thermal environment or density structure lower in the corona that is likely enhancing the C^{4+} possibly by broadening the charge state distribution as evidenced in panel (c). Fe/O increases as well, also suggesting that this wind originates from outside of a coronal hole.

This shock does not seem to be driven by fast solar wind, especially since the composition does not change to reflect low latitude coronal hole properties and the distance of Solar Orbiter (~0.80 au) is likely too close to allow the stream interaction region to steepen into a shock (Jian et al. 2006). While there is a slight increased average charge states of carbon and oxygen suggesting an ICME origin for the shock, there is no clear evidence of a flux rope structure in the MAG data (courtesy SOAR). The lack of an obvious shift to higher Fe charge states,as is often observed within magnetic clouds (Aellig et al. 1998), suggest that either Solar Orbiter does not pass through the hottest part of the ICME or the ICME heating close to the Sun occurred in a region that did not affect the Fe freeze-in. We note that the charge states that are currently provided only include Fe^{8+} to Fe^{12+}, since a refinement of the analysis of higher Fe charge states is still ongoing. It is possible that higher charge states exist during this time interval, but they are simply not visible in the delivered data.

It is worth noting that composition changes occur contemporary to the shock passage (~22:48 UTC). This rapid transition in composition at a shock associated with an ICME has been reported previously, for instance, in Wurz et al. (1998). Furthermore, Kilpua et al. (2017) compared sheath and ICME plasma and found that ICMEs tend to included a pronounced tail towards higher charge states and element abundance ratios; this study also showed that a non-zero fraction of sheath observations can reach $O^{7+}/O^{6+} > 1.0$ and Fe/O > 0.16. Additionally, the shape and thickness of the sheath can vary strongly based on the curvature of the ICME and observational cut through the ejecta. Future investigations into this event can leverage broader Fe charge states to further constrain the thermal history of the solar wind during this event. The distinct changes in the composition pre- and post-shock indicate that the source region or conditions have changed between the two solar wind streams. The sharp increase in $v_{th;O^{6+}}$ suggests local heating at the shock, which is explored in more detail by Alterman et al. (in prep.) with Fe^{8+} to Fe^{12+} during a different shock observed on March 11, 2022.

The second example interval is shown in Fig. 4 for the period from March 8 to 9, 2022 when Solar Orbiter was traveling along its orbit from ~0.480–0.463 AU. This period is characterized by varying solar wind structures, with an ICME with clear composition signatures occurring near 18:00 UTC, marked by a vertical solid black line. The magnetic obstacle associated with this ICME begins just before 22:00 UTC on March 8, 2022 (the first vertical dashed black line) and persists until 08:00 UT on March 9, 2022. The solar wind O^{6+} velocity remains in the range 360–500 km s^{-1} during the entire interval. Based on the O^{6+} velocity and thermal velocity profile, the composition changes, and the boundaries of the magnetic obstacle, the ICME is estimated to have lasted until 08:00 UTC (marked by the second vertical solid black line). The arrival of the shock associated with the ICME corresponds to significant changes in the charge state distributions for C, O, and Fe, with all of them shifting towards higher charge states. The shift to higher charge states has been well documented in literature as a reliable signature of heated ICME material (e.g., see Lepri et al. 2001; Zurbuchen & Richardson 2006, and references therein). There is a clear enhancement of the higher charge states of C, O, and Fe during the first half of the ICME. During the second half, the high charge states are more intermittent, indicating the presence of structures that vary on times scales of 10 s of minutes. The charge state ratios also show enhancement during the ICME period, with the O^{7+}/O^{6+} having the most noticeable increase that lasts throughout the ICME. The Fe/O is enhanced during the first half of the ICME and then returns to slow wind values towards the end of the ICME; it remains there for the duration of the interval, despite some additional structure after the second shock. The structure of the heated material seen in the ICME at a 10 min temporal resolution will provide valuable insights into the thermal history and the source regions of ICME plasma when considered in the context of models of ICME initiation and release.

5. HIS statistics and SWICS comparison

As the solar wind expands out of the solar corona, the freeze-in process occurs as the ionization and recombination processes governing the charge states in radially evolving solar plasma become less and less effective at larger heliocentric distances (Hundhausen et al. 1968). Eventually, the plasma becomes too tenuous for ionization and recombination to continue, resulting in fixed, or frozen-in, charge states after a given heliocentric distance which varies for different ions species. Due to this freeze-in process, ion ratios remain the same just after the solar wind leaves the low corona, well below the distances from the Sun reached by the Solar Orbiter. This allows for a direct comparison of heavy ion statistics throughout the heliosphere outside of this distance. Theoretical freeze-in distances have been predicted to range from 1 to 5 R_{Sun} in the solar wind (Landi et al. 2012; Shen et al. 2017), while extending from 15 to 20 R_{sun} in CMEs

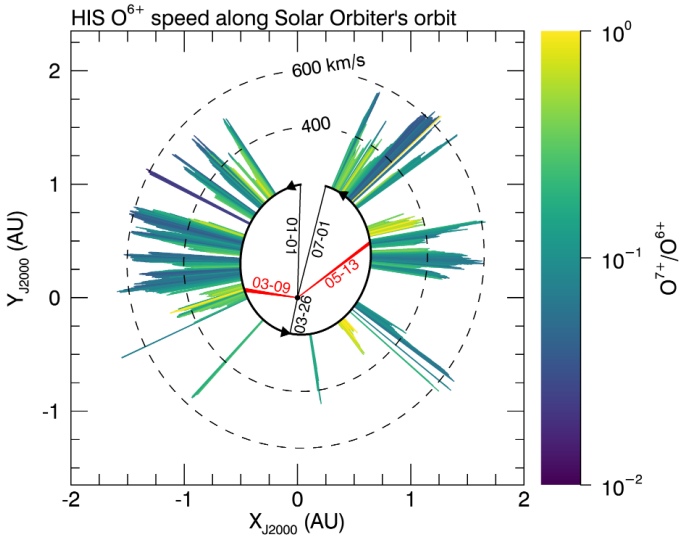

Fig. 5. HIS observations of O^{6+} bulk speed (vector length) and O^{7+}/O^{6+} ratio (vector color) over Solar Orbiter's first science orbit from January–June 2022. Perihelion and interval start+stop dates are labeled in black and the event dates from Figs. 3 and 4 are labeled in red.

(Rivera et al. 2019a). As Parker Solar Probe does not provide such composition measurements, HIS will be the first dedicated instrument to provide mass and charge resolved heavy ions measurements in the solar wind below 1 au, while ACE and Ulysses SWICS observations were taken at 1 au and beyond. Therefore, ions measured by HIS in the inner heliosphere should be generally consistent with those observed with the ACE/SWICS and Ulysses/SWICS instruments at larger heliocentric distances while providing a more detailed view of solar wind substructure and its associated processes.

We find that HIS observations collected to date are in line with the established heavy ion trends previously observed at 1 AU and beyond. Figure 5 shows the orbit of Solar Orbiter from January to June 2022 between ~0.32–1 AU, where the path is in black, the vector length from the path shows the O^{6+} speed, and the vector color indicates the mean O^{7+}/O^{6} value associated with that period. We find that measurements throughout the orbit exhibit a strong correlation between the characteristic solar wind speed and the O ion ratio. Slower speed solar wind contains the highest O^{7+}/O^{6+} values while the ion ratio decreases for higher speed wind. The broad range of values of O^{7+}/O^{6+} observed indicate that Solar Orbiter was intersecting solar wind connected to a range of source regions as it swept through the inner heliosphere (Zhao et al. 2009). We note that the O^{7+}/O^{6+} value is not strictly the same for a specific speed wind but rather a sensitive marker of the varying coronal structures and thermal conditions of where it originated from. Measurements from this nearly full orbit of Solar Orbiter reveal O^{7+}/O^{6+} and other heavy ion properties with unprecedented detail, capturing fine-scale structure in the solar wind that will reveal important details of its birthplace and outflow dynamics.

Figure 6 compares the solar wind's ionic behavior as observed by HIS (left column, panels (a) and (c)) during this orbit with analogous ACE/SWICS observations from 1998–2011 (right column, panels (b) and (d)). The top row plots a 2D histogram of O^{7+}/O^{6+} as a function of O^{6+} speed for HIS (panel (a)) and SWICS (panel (b)). The normalized 1D histogram of the different quantities is shown to the left of each plot. The bottom row plots Fe/O over the indicated charge states for both Fe and O, also as a function of O^{6+} speed in a similar manner for HIS (panel (a)) and SWICS (panel (b)). The 2D histograms of HIS data are collected from January 17, 2022 to June 26, 2022. The figure demonstrates that O^{7+}/O^{6+} ion ratios exhibit their typical anticorrelated speed dependencies, showing higher ratios in the slowest speed wind that gradually decreases with increasing solar wind bulk speed. This relationship is also observed in the 2D histogram of C^{6+}/C^{5+} against O^{6+} speed that is not shown in the figure. The Fe/O element abundance ratio is shown to span from photospheric values, where Fe/O ≈ 0.0589 or $\log_{10}$(Fe/O) = −1.23 (Asplund et al. 2021), to values enhanced by two to three times the photospheric value at slow solar wind speeds (Aellig et al. 1999; Wurz et al. 1999). At higher solar wind speeds, Fe/O is confined to lower values. This resembles the range of values observed by ACE and Ulysses (Stakhiv et al. 2015, 2016).

Figure 7 shows 2D histograms of HIS (panels (a),(c)) and ACE/SWICS (panels (b),(d)) measurements of C^{6+}/C^{5+} versus O^{7+}/O^{6+} and O^{6+} thermal velocity against O^{6+} speed for the same periods as Fig. 6. Panels (a) and (b) show that HIS observes a strong positive correlation between C^{6+}/C^{5+} and O^{7+}/O^{6+} similar to that observed by ACE/SWICS (Zhao et al. 2017b). Additionally, a small fraction of plasma contains ion ratios that fall below the main population are visible in panel (a) and likely represent the same outlier wind as identified in ACE/SWICS measurements (Zhao et al. 2017b; Kocher et al. 2017; Rivera et al. 2021). Zhao et al. (2017b) developed a linear fit to quantify the correlation between C^{6+}/C^{5+} and O^{7+}/O^{6+}, identifying the outlier wind based on solar minimum conditions. This linear relationship is shown by the solid red line in both panels (a) and (b), and the dashed red line marks the upper boundary of the outlier wind (Zhao et al. 2017b). The outlier wind is found to be associated with dropouts first discovered through the notable deviation of the C^{6+}/C^{5+} ratio from its correlated behavior with the O^{7+}/O^{6+} ratio, where the C^{6+}/C^{5+} value appears significantly lower than the statistical trend would suggest. Follow-up studies have found that along with dropouts in C^{6+}/C^{5+}, other bare ions (i.e., ions with mass-per-charge equal to 2 and fully stripped of electrons) are anomalously reduced in the solar wind as well. However, it remains unclear how the plasma becomes depleted of those ions.

The positive correlation between C^{6+}/C^{5+} and O^{7+}/O^{6+} observed in the HIS observations, made just after solar minimum has a similar slope, but is shifted compared to SWICS observations accumulated over a whole solar cycle. This shift to lower ion ratios is likely due to solar cycle effects where ion ratios are generally lower at solar minimum compared to solar maximum (Lepri et al. 2013). This trend is visible in the Zhao et al. (2017b) paper during the ascending phase of the solar cycle, where the majority of the points lie below the 2007 best-fit line. These HIS observations support the idea that the process responsible for the absence of those specific ions in the outlier wind may originate closer to the Sun (Raymond et al. 2022).

The bottom row (panels (c) and (d)) of Fig. 7 shows that the thermal speed of O^{6+} exhibits a correlated speed dependence in accordance to previous observations (Tracy et al. 2015). While the freeze-in process establishes charge state distributions in the plasma within a few solar radii of the Sun, wave-particle interactions and turbulence will continue to influence ion kinetic properties such as their velocities and temperatures as the plasma evolves away from it. For instance, alpha to proton differential streaming, $v_{\alpha,p}$, normalized to the Alfvén speed, C_A, have long been observed to decreases with increasing distance from the Sun, as well as with decreasing solar wind speed

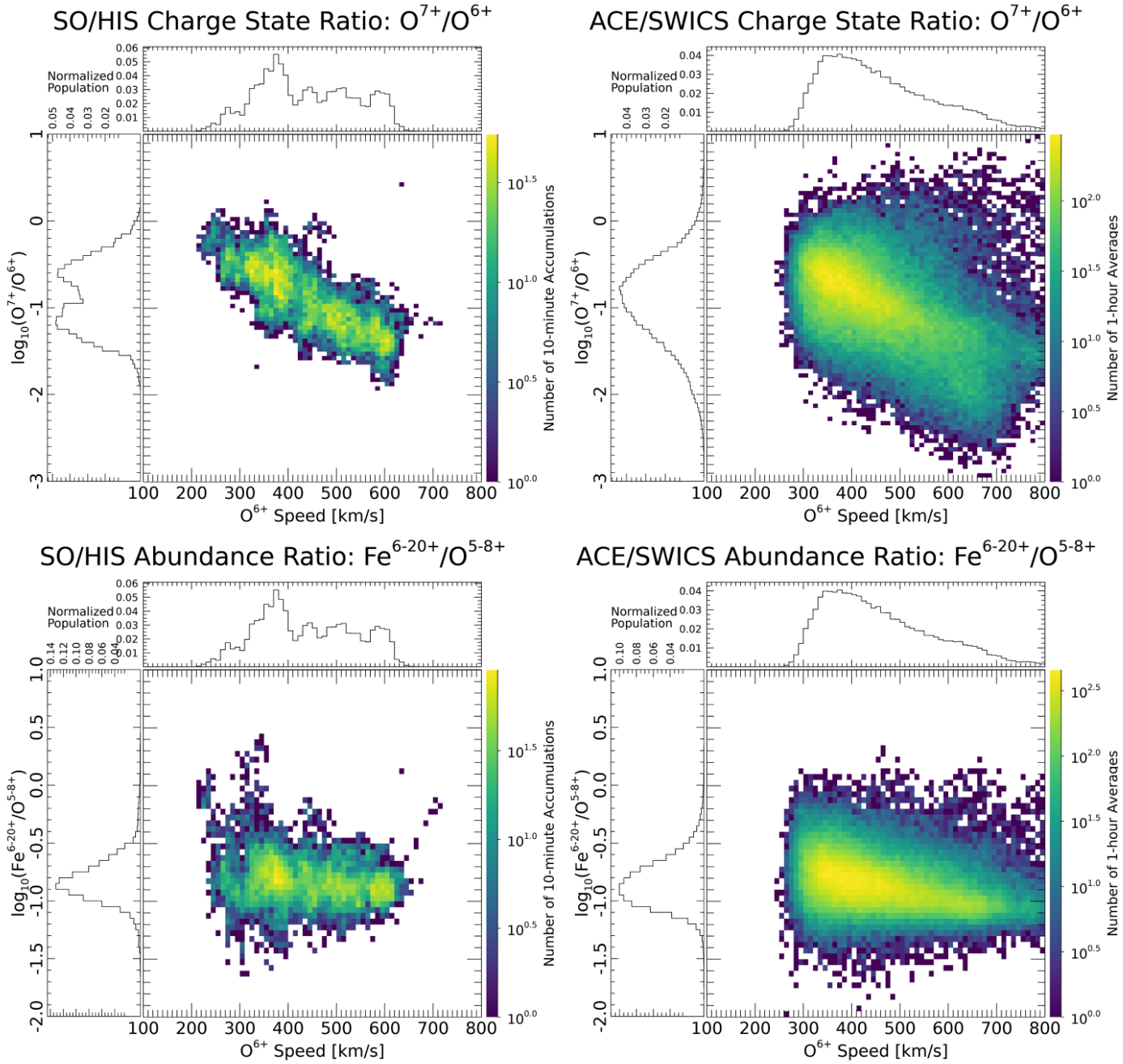

Fig. 6. 2D histograms of Solar Orbiter HIS (left column) and ACE/SWICS (right column) measurements of O^{7+}/O^{6+} ion ratio and Fe/O relative elemental abundance against O^{6+} speed over Solar Orbiter's first science orbit from January to June 2022 and ACE measurements collected between 1998–2011.

(Robbins et al. 1970; Marsch et al. 1982a,b; Neugebauer et al. 1996; Kasper et al. 2017; Alterman et al. 2018). Similarly, heavier ions ($Z > 2$) are observed to differentially stream faster than protons, with an average streaming value of half the local Alfvén speed (Berger et al. 2011). Correspondingly, ion temperatures appear super-mass proportional, where $T_{ion}/T_p > m_{ion}/m_p$ in coronal hole wind, while the large temperature differences among the ions collapses towards the proton temperature in dense, slow speed wind. The reduction of differential streaming and super-mass proportional temperature signatures across solar wind speed and heliocentric distances are often attributed to the strong coupling between ions and protons that ultimately lead to their thermalization (Tracy et al. 2015, 2016). The correlated speed dependence can be observed in O^{6+}, as plotted in Fig. 7, showing the O^{6+} thermal speed rising with increasing solar wind speed. The dependence is most noticeable at lower speeds where the thermal speed climbs sharply from solar wind speeds 200 to 450 km s^{-1} and plateaus toward higher speeds. Note that the O^{6+} thermal speed observed with HIS (panel (c)) throughout the inner heliosphere extends to higher thermal velocities compared to the O^{6+} thermal velocity observed with SWICS (panel (d)) for the same speed wind at 1 au. The higher O^{6+} thermal speed observed with HIS suggests that non-negligible kinetic effects are present between these heliocentric distances.

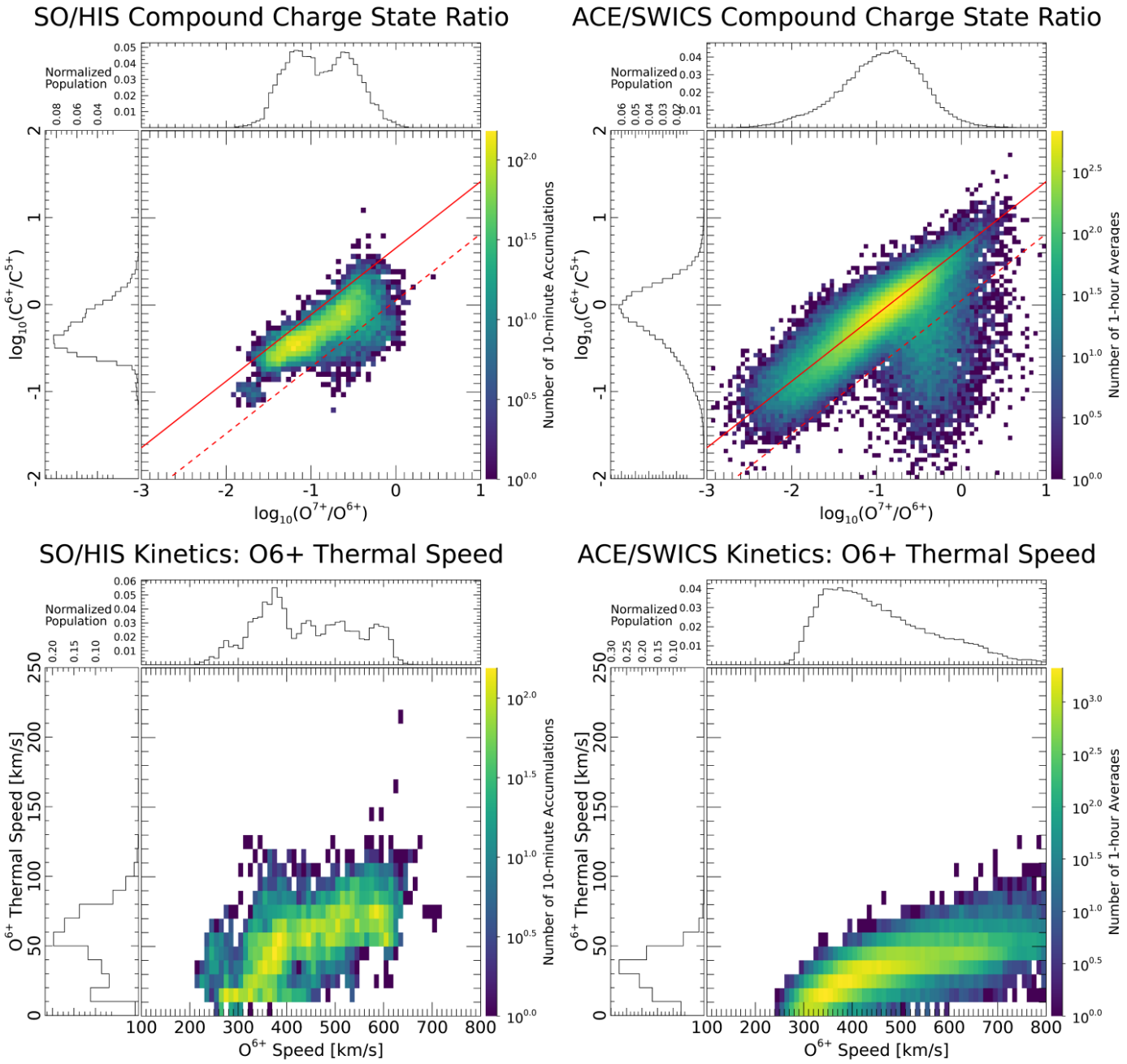

Fig. 7. 2D histograms of Solar Orbiter HIS (left column) and ACE/SWICS (right column) measurements of C^{6+}/C^{5+} versus O^{7+}/O^{6+} ion ratios and O^{6+} thermal velocity against O^{6+} over Solar Orbiter's first science orbit from January–June 2022 and ACE measurements collected between 1998–2011. The red solid and dashed lines in the plots of the top row show the linear fit of all 2007 SWICS data and an empirically selected offset below of the same slope, respectively, as done for Zhao et al. (2017b). The dashed line indicates periods in the solar wind where C^{6+}/C^{5+} ratios fall outside of the typical correlated trend expected to O^{7+}/O^{6+}. The solar wind with C^{6+}/C^{5+} values below the dashed line is the so-called "outlier wind", whose value is lower than expected given an anonymously low C^{6+} abundance (see details in Sect. 5).

6. Discussion and conclusions

In this paper, we present an overview of the first measurements of heavy ion composition from Solar Orbiter's HIS. We described the methods used to transform spectra obtained on board into heavy ion composition parameters that have been made available for public use. We present an overview of two intervals of variable solar wind, whereby ICMEs were identified as embedded and identified by their unique composition. We also examine the statistical nature of the HIS heavy ion measurements collected to date and observe a consistency with prior measurements further out in the heliosphere.

The HIS dataset provides the first mass- and charge-resolved heavy ion measurements within 1 AU. From the accumulation of heavy ions throughout the first perihelion, we find HIS is in good agreement with ionic solar wind trends established from decades of ACE and Ulysses observations at 1 AU and beyond. These provide a basic confirmation of predictions from ion freeze-in theory and coronal observations (Landi et al. 2012; Boe et al. 2018; Gilly & Cranmer 2020) as well as an essential

link between solar wind structures and their source regions on the Sun. Correspondingly, the high temporal resolution available from HIS has the capacity to capture never-before-seen fine-scale solar wind structure enabling a more detailed examination of kinetic effects that are key to understanding the formation and energization of solar plasma (Rivera et al. 2022b). These high temporal resolution data have the potential to transform our understanding of the source, acceleration, and release of plasma out of the solar corona, as well as to deepen our understanding of plasma environments around planets, comets, and the interstellar medium via PUIs.

HIS measurements, when combined with measurements from other ins situ and remote sensing instruments, will help build a more complete picture of the solar wind and its link to the solar corona. For example, the combination of HIS measurements with remote sensing measurements from spectrometers such as Solar Orbiter's SPectral Imaging of the Coronal Environment instrument (SPICE; SPICE Consortium 2020) provide novel opportunities to link solar wind features at the Sun based on their composition properties to differentiate among various physical models of the Sun's atmosphere (Peter 1998; Uzzo et al. 2003; Laming et al. 2019; Réville et al. 2021).

Acknowledgements. Solar Orbiter is a mission of international cooperation between ESA and NASA, operated by ESA. Funding for SwRI was provided by NASA contract NNG10EK25C. Funding for the University of Michigan was provided through SwRI subcontract A99201MO. Funding at University of New Hampshire was provided through SwRI subcontract A99200MO. Solar Orbiter magnetometer operations are funded by the UK Space Agency (grant ST/X002098/1). Tim Horbury is supported by STFC grant ST/W001071/1. Yeimy J. Rivera acknowledges the Future Faculty postdoctoral fellowship from Harvard University. Solar Orbiter SWA work at UCL/MSSL is currently funded under STFC grants ST/T001356/1 and ST/S000240/1.

References

Aellig, M. R., Grünwaldt, H., Bochsler, P., et al. 1998, J. Geophys. Res., 103, 17215
Aellig, M. R., Hefti, S., Grünwaldt, H., et al. 1999, J. Geophys. Res., 104, 24769
Allegrini, F., Wimmer-Schweingruber, R. F., Wurz, P., & Bochsler, P. 2003, Nucl. Instrum. Methods Phys. Res. B, 211, 487
Alterman, B. L., Kasper, J. C., Stevens, M., & Koval, A. 2018, ApJ, 864, 112
Asplund, M., Amarsi, A. M., & Grevesse, N. 2021, A&A, 653, A141
Bame, S. J., Asbridge, J. R., Feldman, W. C., & Kearney, P. D. 1974, Sol. Phys., 35, 137
Bame, S. J., Asbridge, J. R., Feldman, W. C., Fenimore, E. E., & Gosling, J. T. 1979, Sol. Phys., 62, 179
Bamert, K., Wimmer-Schweingruber, R. F., Kallenbach, R., et al. 2002, J. Geophys. Res. Space Phys., 107, 1130
Bamert, K., Kallenbach, R., le Roux, J. A., et al. 2008, ApJ, 675, L45
Berger, L., Wimmer-Schweingruber, R. F., & Gloeckler, G. 2011, Phys. Rev. Lett., 106, 151103
Boe, B., Habbal, S., Druckmüller, M., et al. 2018, ApJ, 859, 155
Burlaga, L. F., & Chao, J. K. 1971, J. Geophys. Res., 76, 7516
Desai, M., & Giacalone, J. 2016, Liv. Rev. Sol. Phys., 13, 3
Desai, M., Mason, G., Dwyer, J. R., et al. 2003, ApJ, 588, 1149
Drews, C., Berger, L., Taut, A., Peleikis, T., & Wimmer-Schweingruber, R. F. 2015, A&A, 575, A97
Drews, C., Berger, L., Taut, A., & Wimmer-Schweingruber, R. F. 2016, A&A, 588, A12
Filwett, R. J., Desai, M., Dayeh, M. A., & Broiles, T. W. 2017, ApJ, 838, 23
Filwett, R. J., Desai, M., Ebert, R. W., & Dayeh, M. A. 2019, ApJ, 876, 88
Galvin, A. B. 1997, Minor Ion Composition in CME-Related Solar Wind (American Geophysical Union (AGU)), 253
Geiss, J., Gloeckler, G., & von Steiger, R. 1996, Space Sci. Rev., 78, 43
Gershman, D. J., Gloeckler, G., Gilbert, J. A., et al. 2013, J. Geophys. Res. Space Phys., 118, 1389
Gilbert, J. A. 2012, Int. Workshop Instrum. Planet. Missions, 1683, 1123
Gilbert, J. A., Lepri, S. T., Rubin, M., Combi, M., & Zurbuchen, T. H. 2015, ApJ, 815, 12
Gilly, C. R., & Cranmer, S. R. 2020, ApJ, 901, 150
Gloeckler, G., & Geiss, J. 1998, Space Sci. Rev., 86, 127
Gloeckler, G., Cain, J., Ipavich, F. M., et al. 1998, Space Sci. Rev., 86, 497
Hefti, S., Grünwaldt, H., Ipavich, F. M., et al. 1998, J. Geophys. Res., 103, 29697
Horbury, T. S., & OBrien, H., Carrasco Blazquez, I. 2020, A&A, 642, A9
Hundhausen, A. J., Gilbert, H. E., & Bame, S. J. 1968, J. Geophys. Res., 73, 5485
Ipavich, F. M., Lundgren, R. A., Lambird, B. A., & Gloeckler, G. 1978, Nucl. Instrum. Methods, 154, 291
Jian, L., Russell, C. T., Luhmann, J. G., & Skoug, R. M. 2006, Sol. Phys., 239, 337
Jian, L. K., Russell, C. T., Luhmann, J. G., & Galvin, A. B. 2018, ApJ, 855, 114
Kasper, J. C., Klein, K. G., Weber, T., et al. 2017, ApJ, 849, 126
Kilpua, E., Koskinen, H. E. J., & Pulkkinen, T. I. 2017, Liv. Rev. Sol. Phys., 14, 5
Kocher, M., Lepri, S. T., Landi, E., Zhao, L., Manchester, W. B. I. 2017, ApJ, 834, 147
Laming, J. M. 2015, Liv. Rev. Sol. Phys., 12, 2
Laming, J. M., Vourlidas, A., Korendyke, C., et al. 2019, ApJ, 879, 124
Landi, E., Gruesbeck, J. R., Lepri, S. T., Zurbuchen, T. H., & Fisk, L. A. 2012, ApJ, 761, 48
Lepri, S. T., & Rivera, Y. J. 2021, ApJ, 912, 51
Lepri, S. T., Zurbuchen, T. H., Fisk, L. A., et al. 2001, J. Geophys. Res., 106, 29231
Lepri, S. T., Landi, E., & Zurbuchen, T. H. 2013, ApJ, 768, 94
Lynch, B. J., Reinard, A. A., Mulligan, T., et al. 2011, ApJ, 740, 112
Manchester, W., Kilpua, E. K. J., Liu, Y. D., et al. 2017, Space Sci. Rev., 212, 1159
Marsch, E., Mühlhäuser, K.-H., Schwenn, R., et al. 1982a, J. Geophys. Res., 87, 52
Marsch, E., Mühlhäuser, K.-H., Rosenbauer, H., Schwenn, R., & Neubauer, F. M. 1982b, J. Geophys. Res., 87, 35
Mason, G., Gold, R. E., Krimigis, S. M., et al. 1998, Space Sci. Rev., 86, 409
Mason, G., Leske, R., Desai, M., et al. 2008, ApJ, 678, 1458
Möbius, E., Lee, M. A., & Drews, C. 2015, ApJ, 815, 20
Müller, D., St Cyr, O. C., Zouganelis, I., et al. 2020, A&A, 642, A1
Neugebauer, M., Goldstein, B. E., Smith, E. J., & Feldman, W. C. 1996, J. Geophys. Res., 101, 17047
Ogilvie, K. W., Bochsler, P., Geiss, J., & Coplan, M. A. 1980, J. Geophys. Res., 85, 6069
Owen, C. J., Bruno, R., Livi, S., et al. 2020, A&A, 642, A16
Peter, H. 1998, Space Sci. Rev., 85, 253
Posner, A., Schwadron, N., McComas, D., Roelof, E., & Galvin, A. 2004, Space Weather, 2, 10
Rakowski, C. E., Laming, J. M., & Lepri, S. T. 2007, ApJ, 667, 602
Raymond, J. C., Asgari-Targhi, M., Wilson, M. L., et al. 2022, ApJ, 936, 175
Réville, V., Rouillard, A. P., Velli, M., et al. 2021, Front. Astron. Space Sci., 8, 2
Rivera, Y. J., Landi, E., Lepri, S. T., & Gilbert, J. A. 2019a, ApJ, 874, 164
Rivera, Y. J., Landi, E., & Lepri, S. T. 2019b, ApJS, 243, 34
Rivera, Y. J., Landi, E., Lepri, S. T., & Gilbert, J. A. 2020, ApJ, 899, 11
Rivera, Y. J., Lepri, S. T., Raymond, J. C., et al. 2021, ApJ, 921, 93
Rivera, Y. J., Raymond, J. C., Landi, E., et al. 2022a, ApJ, 936, 83
Rivera, Y. J., Higginson, A., Lepri, S. T., et al. 2022b, Front. Astron. Space Sci., 9, 1056347
Robbins, D. E., Hundhausen, A. J., & Bame, S. J. 1970, J. Geophys. Res., 75, 1178
Shearer, P., von Steiger, R., Raines, J. M., et al. 2014, ApJ, 789, 60
Shen, C., Raymond, J. C., Mikić, Z., et al. 2017, ApJ, 850, 26
SPICE Consortium (Anderson, M., et al.) 2020, A&A, 642, A14
Stakhiv, M., Landi, E., Lepri, S. T., Oran, R., & Zurbuchen, T. H. 2015, ApJ, 801, 100
Stakhiv, M., Lepri, S. T., Landi, E., Tracy, P., & Zurbuchen, T. H. 2016, ApJ, 829, 117
Taut, A., Berger, L., Drews, C., & Wimmer-Schweingruber, R. F. 2015, A&A, 576, A55
Tracy, P. J., Kasper, J. C., Zurbuchen, T. H., et al. 2015, ApJ, 812, 170
Tracy, P. J., Kasper, J. C., Raines, J. M., et al. 2016, Phys. Rev. Lett., 116
Uzzo, M., Ko, Y., Raymond, J., Wurz, P., & Ipavich, F. M. 2003, ApJ, 585, 1062
Viall, N. M., & Borovsky, J. E. 2020, J. Geophys. Res. Space Phys., 125, e2018JA026005
von Steiger, R., & Zurbuchen, T. H. 2011, J. Geophys. Res. Space Phys., 116, A01105
von Steiger, R., Schwadron, N. A., Fisk, L. A., et al. 2000, J. Geophys. Res., 105, 27217
Wurz, P., Ipavich, F. M., Galvin, A. B., et al. 1998, Geophys. Rev. Lett., 25, 2557
Wurz, P., Aellig, M. R., Ipavich, F. M., et al. 1999, Phys. Chem. Earth C, 24, 421
Wurz, P., Bochsler, P., & Lee, M. A. 2000, J. Geophys. Res., 105, 27239

Yu, J., Berger, L., Drews, C., Wimmer-Schweingruber, R., & Taut, A. 2018, A&A, 615, A126
Zel'dovich, M. A., Logachev, Y. I., Surova, G. M., & Kecskeméty, K. 2014, Astron. Rep., 58, 399
Zel'dovich, M. A., Logachev, Y. I., & Kecskeméty, K. 2018, Sol. Phys., 293, 21
Zhao, L., Zurbuchen, T. H., & Fisk, L. A. 2009, Geophys. Rev. Lett., 36, L14104
Zhao, L., Landi, E., Lepri, S. T., et al. 2017a, ApJ, 846, 135
Zhao, L., Landi, E., Lepri, S. T., et al. 2017b, ApJS, 228, 4
Ziegler, J. F. 2004, Nucl. Instrum. Methods Phys. Res. B, 219, 1027
Zurbuchen, T. H., & Richardson, I. G. 2006, Space Sci. Rev., 123, 31
Zurbuchen, T. H., Fisk, L. A., Gloeckler, G., & von Steiger, R. 2002, Geophys. Rev. Lett., 29, 1352
Zurbuchen, T. H., Weberg, M., von Steiger, R., et al. 2016, ApJ, 826, 10

[1] Space Science and Engineering, Southwest Research Institute, 6220 Culebra Rd., San Antonio, TX 78238, USA
[2] University of Michigan, Department of Climate and Space Sciences & Engineering, Climate and Space Research Building, 2455 Hayward St., Ann Arbor, MI 48109, USA
e-mail: slepri@umich.edu
[3] Center for Astrophysics | Harvard & Smithsonian, 60 Garden Street, Cambridge, MA 02138, USA
[4] NASA Goddard Space Flight Center, Heliophysics Division, 8800 Greenbelt Road, Greenbelt, MD 20771, USA
[5] NASA Goddard Space Flight Center, Solar System Exploration Division, 8800 Greenbelt Road, Greenbelt, MD 20771, USA
[6] Physics Institute, University of Bern, Sidlerstrasse 5, 3012 Bern, Switzerland
[7] Institut de Recherche en Astrophysique et Planétologie, 9, Avenue, du Colonel ROCHE, BP 4346, 31028 Toulouse Cedex 4, France
[8] University of New Hampshire, Space Science Center, 8 College Rd, Durham, NH 03824, USA
[9] University College London, Department of Space and Climate Physics, Mullard Space Science Laboratory, Holmbury St. Mary, Dorking, Surrey RH5 6NT, UK
[10] Imperial College London, South Kensington Campus, London SW7 2AZ, UK
[11] INAF-IFSI, Via del Fosso del Cavaliere 100, 00133 Rome, Italy
[12] Heliospheric Physics Lab. Heliophysics Science Division, NASA-Goddard Space Flight Center., 8800 Greenbelt Rd., Greenbelt, MD 20770, USA